International Journal of Precision Engineering and Manufacturing-Green Technology (2024) 11:833–847
https://doi.org/10.1007/s40684-024-00610-2

Online ISSN 2198-0810
Print ISSN 2288-6206

REGULAR PAPER

Enhanced Wear Properties of an Inspired Fish-Scale Film Structure in Terms of Microstructured Self-Lubrication Induced Effects by High-Speed Laser Surface Remelting Processing

Wei Dai[1,2,3] · Chuqiao Fang[1,2] · Xiao Wu[1,2] · Zhizhen Zheng[3] · Jianjun Li[3]

Received: 30 November 2023 / Revised: 16 February 2024 / Accepted: 20 February 2024 / Published online: 27 March 2024

Abstract

DC53 tool steel has potential applications in mold product manufacturing because of its excellent toughness properties. However, it suffers from poor wear resistance, which limits its wide range of applications. A micron-size fish-scale film structure was designed on the DC53 steel surface and fabricated using crossover laser surface remelting processing to improve its tribological properties. Three kinds of DC53 surfaces, including the as-received, quenched, and fish-scale film structure, were used to evaluate the tribological properties. Specifically, tribological performance was evaluated using a reciprocating sliding tester. The unidirectional ball-on-disc method was employed to assess the wear of the mating surfaces under low-, medium-, and high-load conditions in terms of friction and wear tests. The friction coefficient and the wear rate were recorded to investigate the formation mechanism of tribo-layers. Experimental results demonstrated that the structure combined with microbulges on the DC53 surface had excellent load-bearing capabilities and wear resistance. Energy dispersive spectroscopy following wear tests showed pronounced material transfer from the structured surfaces, with SiO_2 particles filling up some groove voids. The reinforcing layer in the form of nanoscale SiO_2 particles exhibited enhanced performance at higher tribological loads. The synergistic effects of microbulges and SiO_2 films significantly improved the tribological properties of DC53 materials. In addition, the precipitation of SiO_2 contributed to the anti-wear performance of the tool steel surface, which is consistent with the self-lubricating wear mechanism of the worn surface. The laser surface remelting technique enables the fabrication of a micro fish-scale film structure, which has great potential for enhancing the wear resistance and applications of DC53 materials in various fields.

Keywords DC53 tool steel · Film structure · SiO_2 · Self-lubrication · Wear resistance

1 Introduction

DC53 tool steel has excellent toughness and fatigue resistance, good electrical discharge machining properties [1, 2], nice mechanical machinability [3, 4] and low production costs. At present, it is widely used in manufacturing diecasting and plastic tools in the die and mold industry. However, its relatively poor wear properties limit its wider application potential [5, 6].

Traditional method to enhance the wear resistance of DC53 steel is through surface modification processes such as surface quenching [7], boronizing [5], combined shot and nitriding [8], plasma nitriding, thermal diffusion (TD) carbide and quality conditioning treatment [9], physical vapor deposition [10], and chemical vapor deposition coating. These drawbacks encompass inadequate interfacial adhesion, limited coating thickness, and susceptibility to

✉ Wei Dai
daiw@hust.edu.cn

✉ Xiao Wu
xiaowu@wtu.edu.cn

✉ Jianjun Li
jianjun@hust.edu.cn

[1] Hubei Key Laboratory of Digital Textile Equipment, Wuhan Textile University, Wuhan 430200, China

[2] School of Mechanical Engineering & Automation, Wuhan Textile University, Wuhan 430200, China

[3] State Key Laboratory of Materials Processing and Die & Mould Technology, College of Materials Science and Engineering, Huazhong University of Science and Technology, Wuhan 430074, China

damage or delamination during repetitive thermal cycles [8, 9], which necessitates the exploration and investigation of novel methodologies.

Currently, the demand for functional structured surfaces [11, 12] is increasing in terms of high wear resistance [13] and low friction coefficient [14]. The structured surface refers to micro-size topographies with specific scales arranged in certain orders [15, 16]. In addition, its main characterization parameters, including the geometric shape [17, 18], depth and distribution [19, 20], can reduce wear resistance.

Traditional processing methods can no longer meet the diverse requirements for preparing structured surfaces. However, with the development of laser technology, the quantized surface structured by laser irradiation [21, 22] and laser shock peening [23, 24] can improve the surface friction performance. In recent years, a new metallic structured surface created by laser remelting [25, 26] has attracted great scientific attention. Unlike traditional laser-structured surfaces, this technology represents innovation by eliminating ablation [27, 28] and allowing material redistribution through melting [29–31] without the need for removal. This leads to non-mechanical stress on the treated components.

Inspired by improved wear properties owing to the bionic surface morphology on DC53 steel, a fish-scale film structure was fabricated through the cross-over laser surface remelting process. This research aimed to address the lack of systematic evaluation regarding the frictional characteristics and wear mechanisms that significantly influence the output wear properties in DC53 steel. In addition, the bionic surface morphology of the fish-scale film structure has not been thoroughly investigated, as recommended in the literature. Thus, it could potentially offer superior outcomes compared to previously established methods. The wear behaviors and mechanism of the fish-scale film structure were also evaluated to resolve this problem and improve the state of the art.

2 Experimental Details

2.1 Experimental Materials

Commercial JIS DC53 tool steels with toolbars (0.95 C, 1.00 Si, 0.40 Mn, 8.00 Cr, 2.00 Mo, 0.30 V, and Fe, all balanced in wt. %) were selected as the experimental materials. Prefabricated specimens were machined to the dimensions of $20\times20\times20$ mm^3 by electrode discharge machining (EDM) with a surface roughness $\boldsymbol{R_a}$ of 3.60 µm. They were rinsed with alcohol and dried as the as-received specimens after being degreased and ultrasonically cleaned.

2.2 Quenching Processing

To exclude changes in wear resistance caused by quenching action, surface quenching processed DC53 tool steel was also used as the compared specimens on the following parameters: Quenching treatment at 1,030 °C for 60 min, tempering treatment at 300 °C for 120 min, and air cooled. Thereafter, the surface was polished by grinding, and the roughness $\boldsymbol{R_a}$ of 0.2 µm was used for the wear test on quenched specimens.

2.3 Laser Remelting Assisted Surface Structuring

The fiber laser (IPG YLR-300-LP, IPG Photonics) with the TEM_{00} mode was used for the laser remelting process. Its wavelength, beam spot diameter, and maximum output power were 1,070–1,080 nm, 50 µm, and 300 W, respectively. The HurrySCAN-10 scanning galvanometer (ScanLAB, Germany) was used for high-speed laser scanning. Table 1 shows the processing parameters for the laser surface remelting experiment.

The process of the formation of the micron-sized fish-scale film structure in the work is based on the superficial melting of surface materials. As shown in Fig. 1a, a thin surface layer is melted by laser radiation. The melt pool is relocated by the surface tension and the molten material solidifies. The role of laser beams in scanning the steel surface is demonstrated by their ability to significantly enhance the heat transfer to the molten pool. The second reason is the disruption of the solid–liquid interface and flowing melt, namely mass transfer. This is the main reason why the inclusion is continuously pushed to the edge of the molten pool. The heat source of the laser plays a crucial role by exerting buoyancy and surface tension that promotes the formation of the molten pool.

When the heat flows vertically from the inside of the molten pool to the outside, the surface tension at the edge is greater than in the center. Therefore, surface tension causes inclusions flow to the edge of the melt pool. As shown in Fig. 1b, when the two scanning profiles of laser beams overlap each other, the previously melted scanning

Table 1 Laser processing parameters on DC53 steel

Type	Data
Laser power (W)	300
Scan speed (mm/s)	100–200
Defocus (mm)	0
Spot size (µm)	50
Scan cross angle (°)	60
Protected gas	Ar (99.999%)

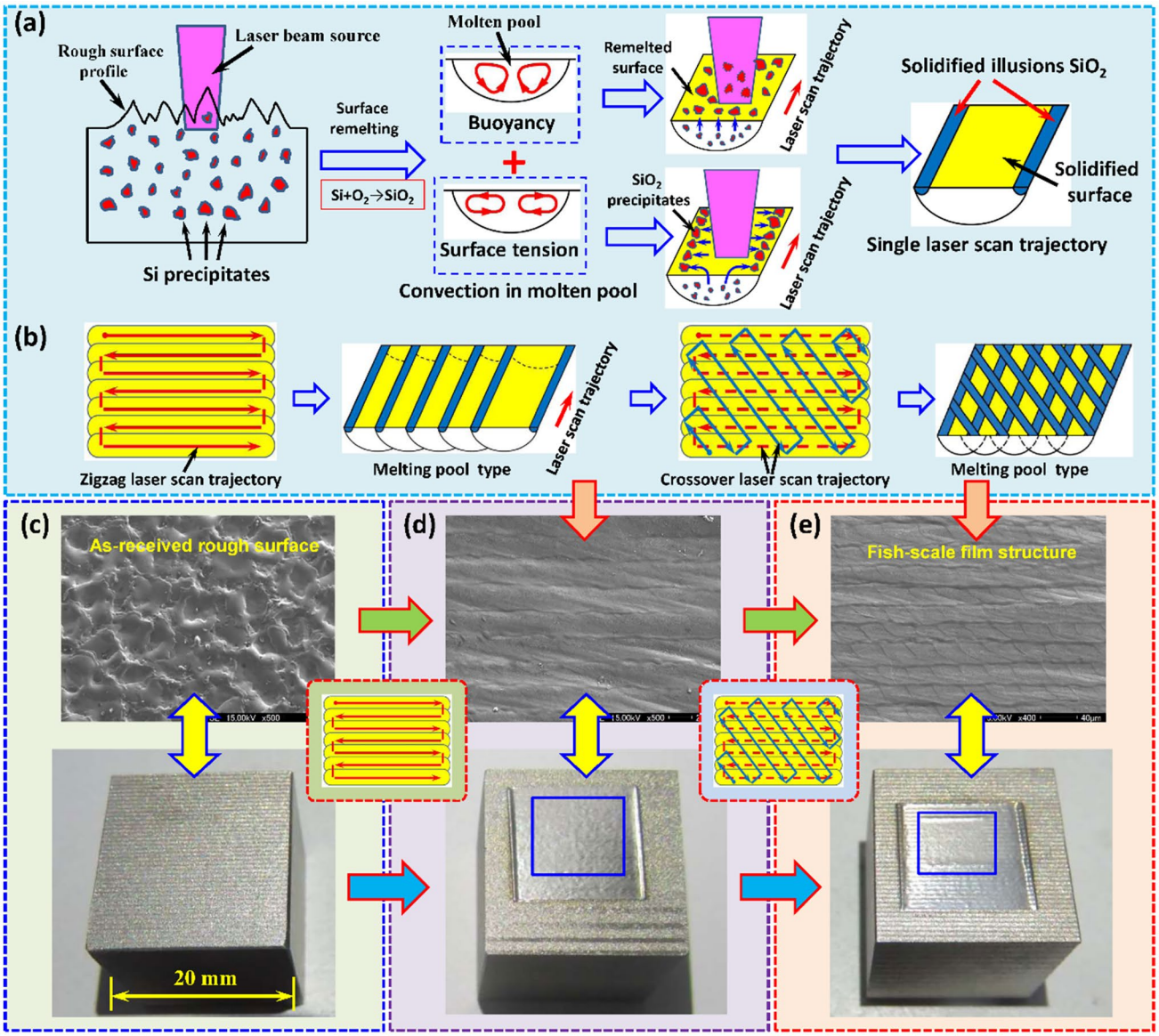

Fig. 1 Laser fabrication process of inspired fish-scale film structure: **a** fish-scale film structure induced by laser surface remelting; **b** structure formation by cross-over laser scanning trajectory [32]; **c–e** as-received, the first and crossed laser beams scanned specimens and the corresponding surface morphologies

track section is recrossed by the second laser beam and melted again to obtain a regularly distributed fish-scale film structure with quadrilaterals. The as-received, the first and second crossed laser beam scanned specimens and the corresponding surface morphologies are shown in Fig. 1c–e, respectively.

2.4 Wear Behaviors Tests

Tribological behaviors were investigated under dry conditions using a conventional ball-on-plate tribometer (Bruker UMT-2 TriboLab) (Fig. 2). The upper friction pair consisted

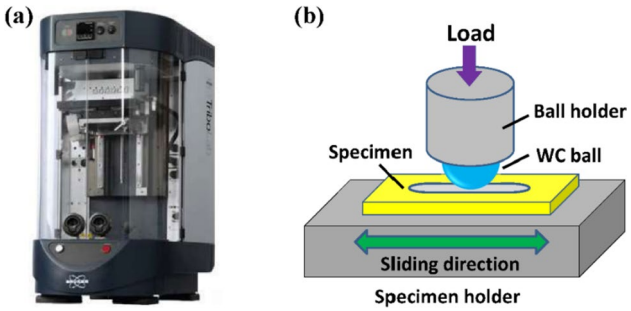

Fig. 2 Wear test equipment: **a** UMT-2 wear test machine; **b** Ball-on-plate wear test structure

of a high-hardness tungsten carbide (WC) ball with a diameter of 5.0 mm and an R_a of 0.05 µm. It performed the reciprocating sliding motion against the specimens at a linear speed of 10 mm/s and a sliding distance of 10 mm. The wear resistance of specimen surfaces was evaluated by applying three static loads (10, 20, and 50 N) twice under controlled environmental conditions (temperature: 25 ± 2 °C and relative humidity: 50 ± 5%) for a constant test duration of 150 min. The work aimed to evaluate the overall wear resistance of the fish-scale film structure surface. It was not necessary to explicitly specify the sliding direction of the upper friction pair because it is related to the texture orientation angle on the sample surface in friction experiments.

The contact surface of the tool and specimen was cleaned with ethanol before the experiment. The relationship between the friction coefficient and the test duration was continuously recorded during the tests and compared with the surface of the as-received, quenched, and fish-scale film structure under equivalent conditions. The main tribological properties were studied in terms of friction coefficient, wear volume loss, worn surface morphology, and element distribution of each specimen under different loads.

2.5 Surface Characteristics

Surface morphology was analyzed using the Quanta 200 scanning electron microscope (SEM), and composition distribution was recorded by energy dispersive spectrometer (EDS) and electron probe microanalysis (EPMA-8050G, Shimadzu, Japan). Auger electron spectroscopy (AES) and X-ray photoelectron spectroscopy (XPS) were used to check the element distribution, chemical composition and concentration of the worn fish-scale film structure. AES measurements (PHI Auger 710 Nano) were carried out at 8.0×10^{-8} Pa, the primary electron beam energy of 10 kV, a probe current of 50 nA, and an incident angle of 30°. Element distribution was analyzed by Ar^+ sputtering with the primary electron beam of 2 keV and an ionic current of 0.5–2 µA. A standard silica plate was calibrated at a sputtering rate of 25 nm/min. Sputtering depth was tested up to 3,000 nm, with the recorded depth for each iteration being 100 nm. The XPS test (AXIS-ULTRA DLD-600W) was carried out at a vacuum pressure of 5.5×10^{-8} Pa. Narrow-spectrum scanning was performed using Al Kα x-rays (1486.6 e; the total resolution of 0.5 eV) at an operating parameter of 10 kV voltage and 200 W. The scanning step accuracy of the detector was 0.1 eV, and all chemical binding energies were calibrated by C1s (284.60 eV) as the standard. In addition, worn surface morphology was analyzed by the SEM, and the 3D worn surface volume loss was recorded using a laser confocal microscope (LSCM, VK-X200, Keyence).

3 Results and Discussions

3.1 Surface Morphology

Figure 3 shows the surface morphology of EDM-processing and fish-scale film structure of DC53 steel. Figure 3a–c show the macro- and microscopic appearance of the tailored

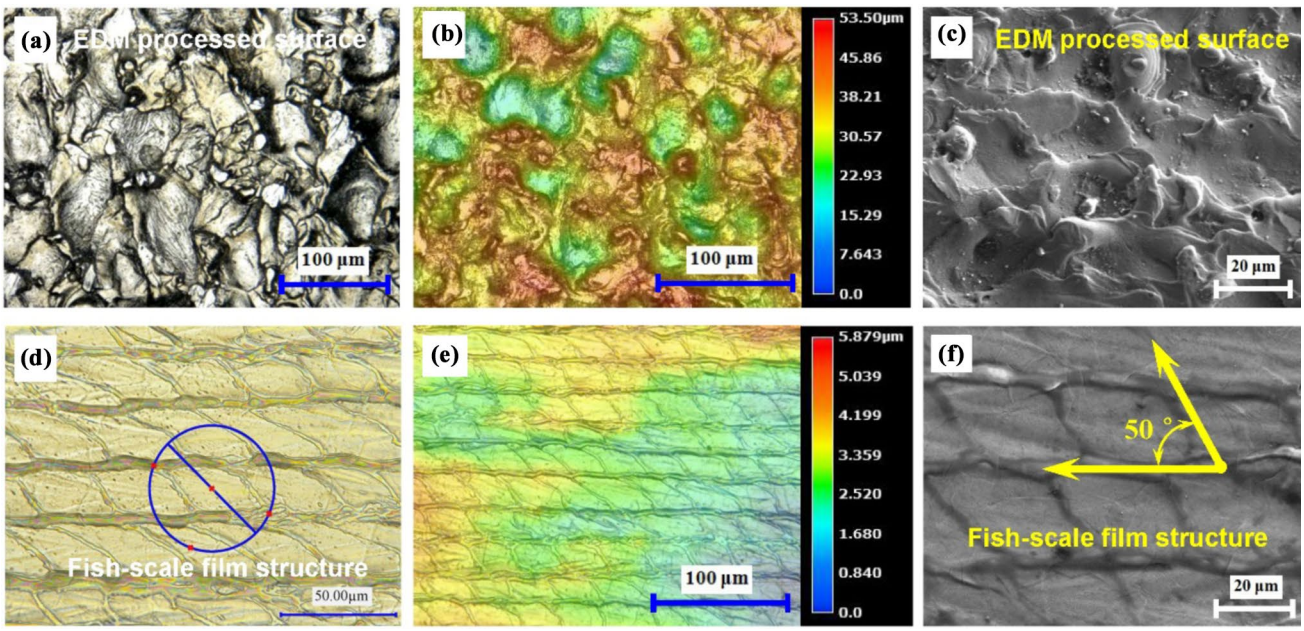

Fig. 3 Compare the optical microscopy, height profile and SEM morphology results of **a–c** as-received; **d–f** fish-scale film structure specimen

rough surface after EDM. The structure is formed through laser surface remelting using crossed laser galvanometer scanning, and exhibits a periodic array of non-smooth fish-scale film structures (Fig. 3d–f). The scales have an irregular quadrilateral outline. The scale groove is convex and runs parallel to the scale edge.

EPMA surface mapping scanning was used to examine the element distribution of the structure composition (Fig. 4). Si and O (Fig. 4b–c) are mainly concentrated in the imbricate groove, while other elements are not obvious. The morphology and element distribution characteristics of the fish-scale film structure provide potential opportunities to improve its wear resistance.

3.2 Wear Behavior of the As-Received Surface

Figure 5 presents the SEM images for the influence of wear loads on the worn surface morphology of as-received DC53 steel. As the wear load increases, the number of worn surfaces increases. The worn surface deforms slightly under a load of 10 N and shows some abrasion marks caused by loose worn particles. Figure 5a shows a relatively flat worn surface caused by light abrasive wear. As load increases to 20 and 50 N, a greater number of rough worn surfaces are observed. Some exhibit partially filled dimples and grooves in the spall area (Fig. 5b–c). This indicates the formation of worn surfaces, characterized by increased number of abrasive particles, abrasion debris, and deep pits.

The frictional contact point of the as-received surface can be destroyed under the increased load. The missing protective layer will damage the contact point. As wear loads increase, the amount of worn materials increase significantly, contributing to the formation of rough worn surfaces. Transferred layers (Fig. 5d–e) reveal wear debris and are supported by line scanned EDX analysis confirming Fe, O, and C as major constituting elements. O in the elemental compositions indicates that both trapped and loose wear debris have undergone partial oxidation. Due to the formation of broken discontinuous oxide films on the worn surface, the worn contact surface separates from the metal substrate, resulting in oxide-aggravating abrasive wear.

3.3 Wear Behavior of the Quenched Surface

The worn surface morphology of quenched specimens is different from that of as-received. A slight furrow track forms, with no obvious observed abrasive wear (Fig. 6a). As the load increases, the depth of the plow increases (Fig. 6b–c), and typical plow wear occurs on the worn surfaces.

Elastoplastic deformations occur in the quenched layer due to the quenching process. This layer reduces direct contact between the reinforced substrate and the coupled wear materials, which reduces the adhesive effect. The quenched surface exhibits a subtle worn appearance with faint grooves at lower loads. As the load increases, larger indentations form due to the plowing effect. The worn surface undergoes

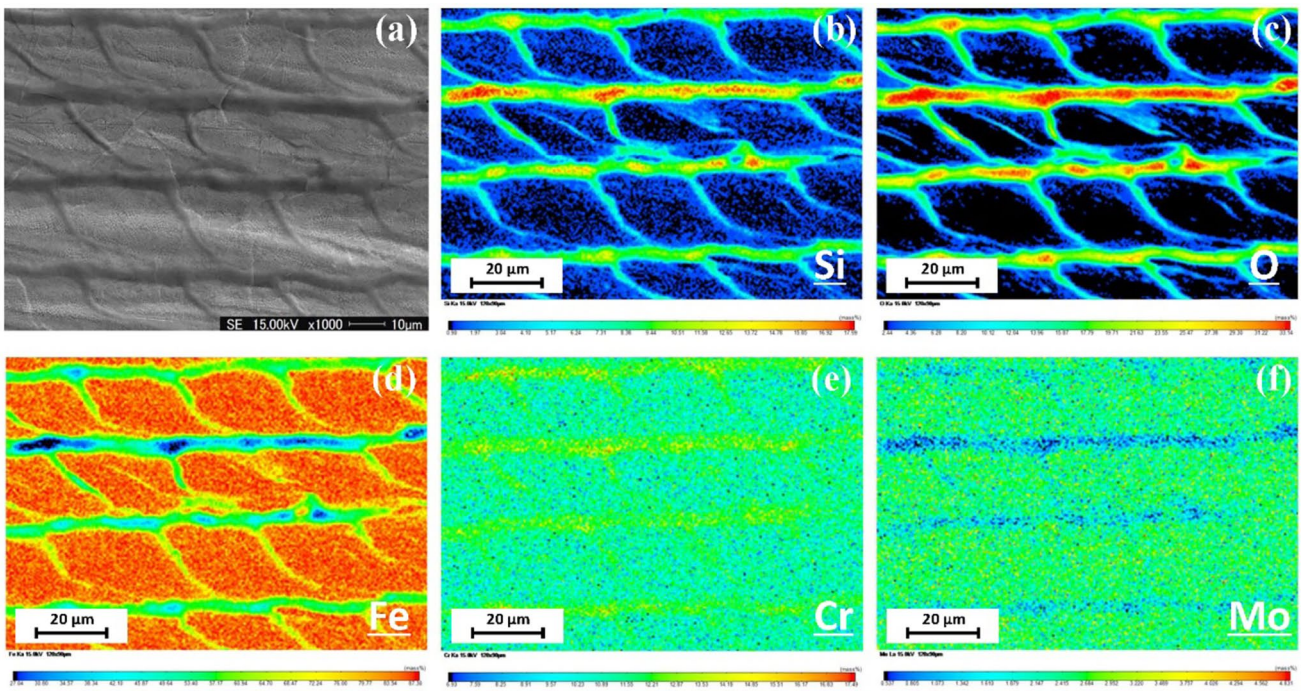

Fig. 4 EPMA element mapping results of fish-scale film structure: **a** surface mapping area; element results of **b** Si, **c** O, **d** Fe, **e** Cr, and **f** Mo

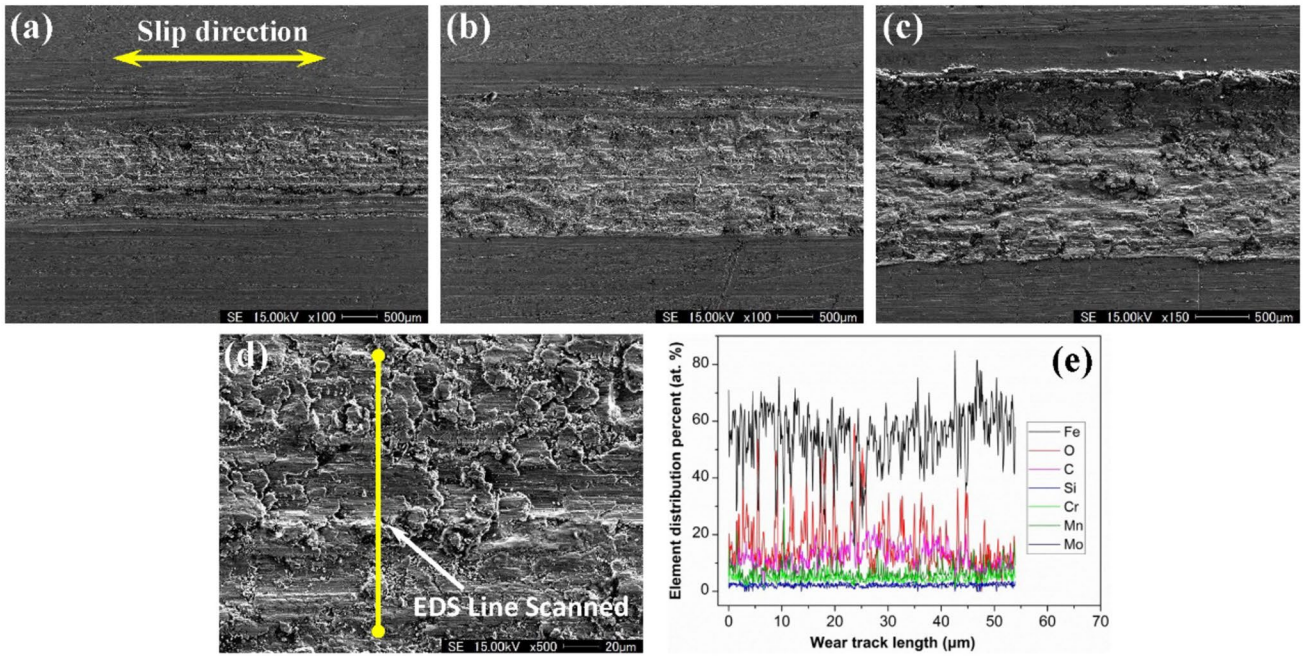

Fig. 5 Worn surface morphology of the wear tracks developed on the as-received DC53 steel at a load of: **a** 10 N, **b** 20 N, **c** 50 N; **d** Enlarged view of the transferred layers at a load of 50 N; **e** EDS results of the transferred layers at a load of 50 N

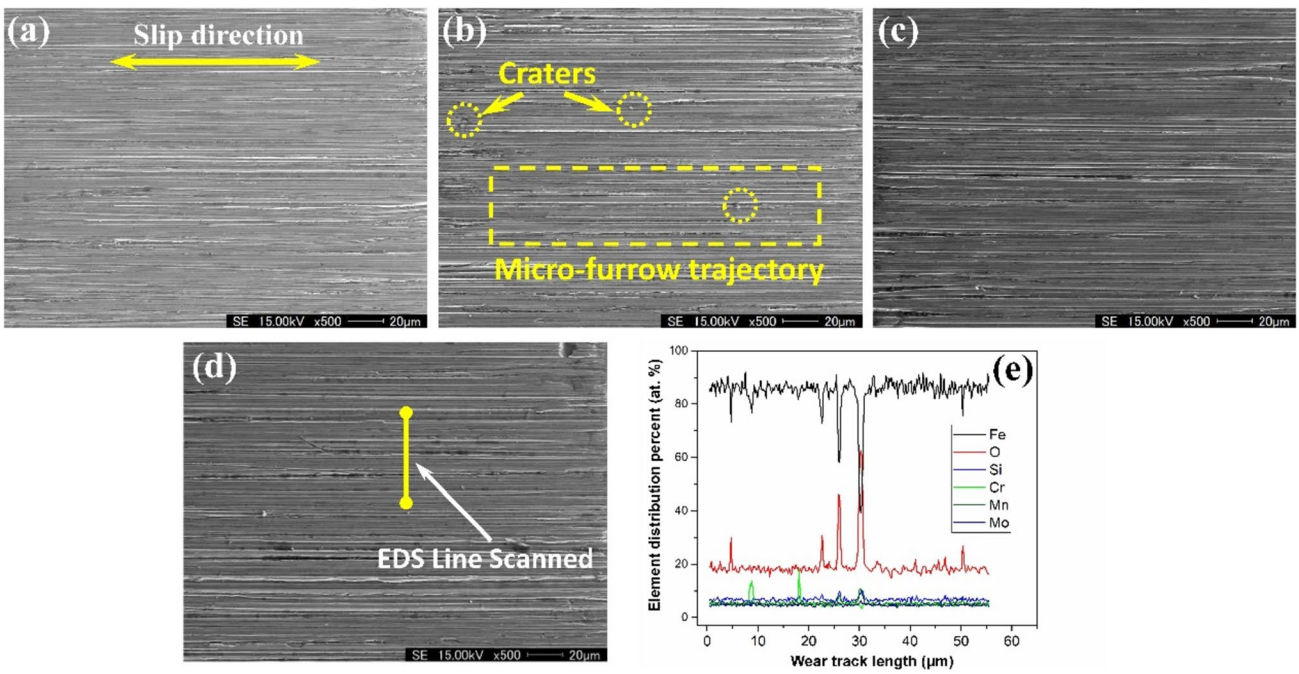

Fig. 6 Worn surface morphology of the wear tracks developed on the quenched DC53 steel: **a** 10 N; **b** 20 N; **c** 50 N; **d** EDS line scanned direction at a load of 50 N; **e** EDS results of the worn layers at a load of 50 N

strong elastoplastic deformation with large protrusions. EDX analysis with corresponding data confirms that Fe and O are the main components (Fig. 6e). This is due to the intense frictional contact and oxidation in the worn transferred layers of the quenched DC53 steel under high loads.

3.4 Wear Behavior of the Fish-Scale Film Structure Surface

A shallow wear track is observed with a relatively flat worn surface and a distinct fish-scale film structure (Fig. 7a). The decrease in worn volume is less than that of as-received and quenched specimens as delivered.

As the load increases, the worn surface remains relatively flat, showing smoother surfaces (Fig. 7b–c). The wear debris in the worn layer is less than that on the as-received and quenched surfaces. The fish-scale film structure with good wear resistance can better resist the reciprocating effect of high loads.

Elements and chemical compositions for the worn surface are identified to recognize the anti-friction mechanism for the fish-scale film structure. The EDS line scanned results show the SiO_2 component at the boundary of the fish-scale film structure (Fig. 7d–e) with good wear resistance. The composition of the structure is confirmed through comprehensive analysis using EPMA, AES, and XPS to image the worn surface elements and analyze the chemical compositions in both superficial and deep layers.

3.5 Worn Surface Elements and Chemical Compositions

EPMA test provides short test duration and extensive coverage, which is more suitable for film layer analysis. Figure 8 shows the EPMA surface mapping scanned results of the worn surface. There are lots of small wear particles, and some coated friction film layers similar to island transfer on the worn surface. The tested surface exhibits the pronounced enrichment of Si (indicated by the dark red color in Fig. 8d) and O (Fig. 8e). Compared with Fe (green part in Fig. 8c), the spreading effect of Si and O on the worn surface can be observed. The preliminary conclusions from EMPA results indicate SiO_2 protective films on the worn surface.

Figure 9 depicts the AES spectra of the worn fish-scale film structure. Figure 9a shows Si, O and Fe at the depth of 1,000 nm, and Si and O spectra at 1,607.63 and 531.81 eV, respectively. Variations in the Si and O content of the worn film in the thickness direction are determined by Auger depth profiling, with depth profiling recorded from 50 to 3,000 nm (Fig. 9b). The average atomic proportions of Si and O in the measured standards are 32.01 and 52.03%, respectively, after the quantitative correction was performed three times using the average atomic proportions of the checked elements.

Elemental compositions obtained from AES depth profiles indicate the atomic percentages of Si and O remain relatively constant with depth in 50 to 3000 nm. In addition, the concentration of Si and O in the tested superficial surface layer is higher than that at a depth of larger than 200 nm. AES results indicate that the worn film structure is attributed to Si and O element in the superficial layer.

The subsequent XPS analysis is used to confirm the chemical formula of the worn surface for the fish-scale film

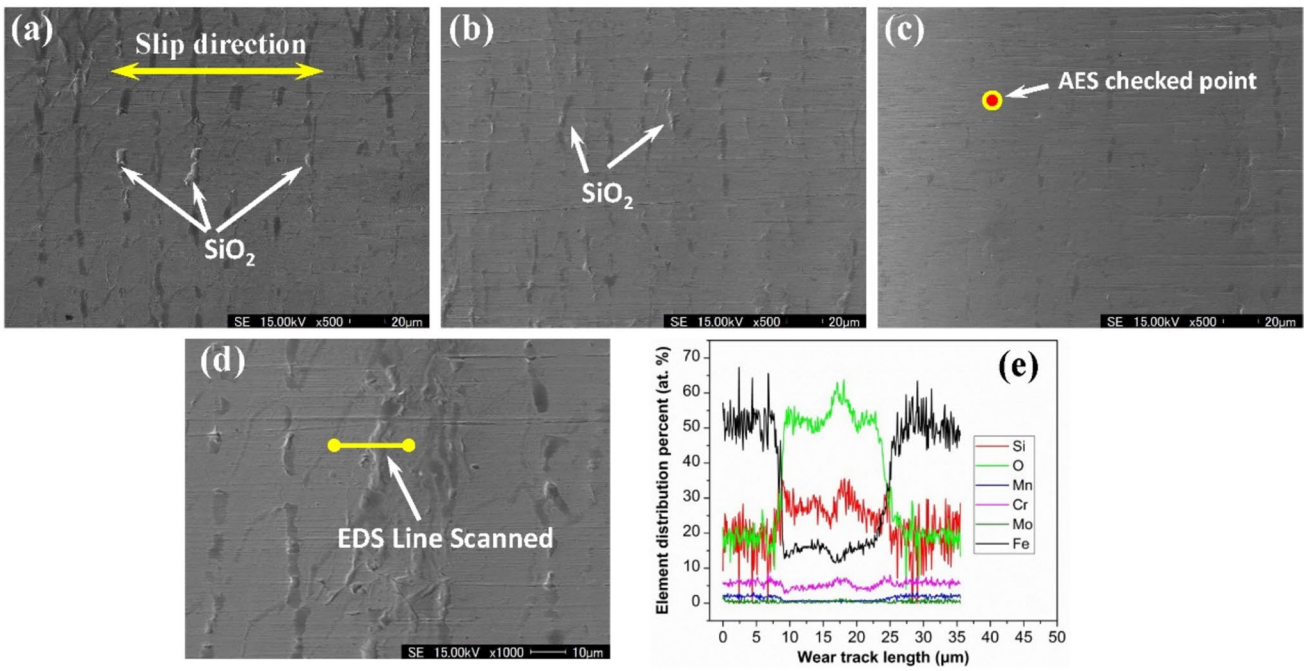

Fig. 7 Worn surface morphology of the wear tracks developed on the fish-scale film structure: **a** 10 N, **b** 20 N, **c** 50 N; **d** Enlarged view of the worn surface at the load of 50 N; **e** EDS results of the worn surface at the load of 50 N

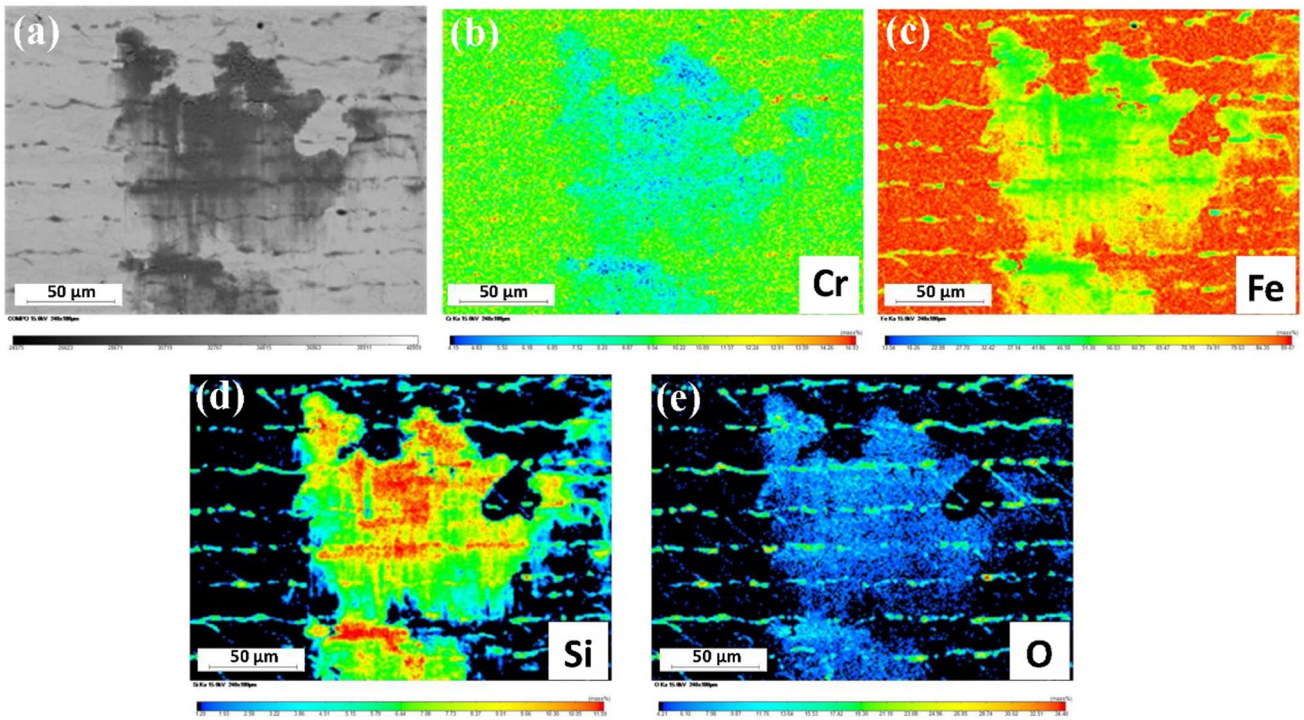

Fig. 8 EPMA element mapping results for the worn fish-scale film structure: **a** SEM morphology with the worn surface mapping area; **b** Cr scan result; **c** Fe, **d** Si, **e** O

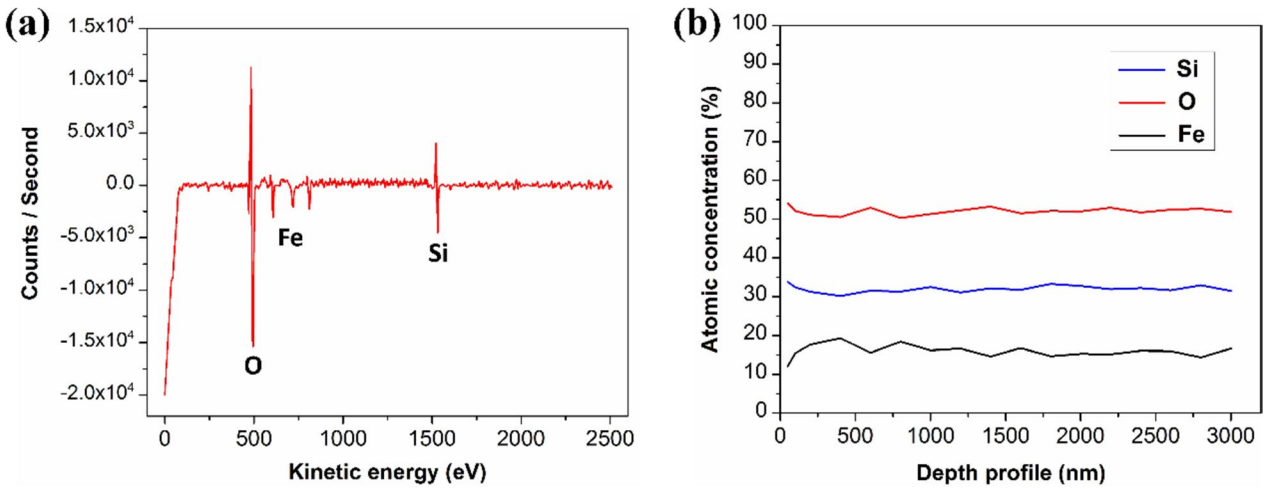

Fig. 9 AES results of the worn fish-scale film structure: **a** Elemental spectra with a resolution at the depth of 1000 nm; **b** Element distributions in the depth profile

structure. Figure 10a presents the XPS wide-scanning profile of the fish-scale film structure, revealing Fe, O, Si, and C on the surface. However, the detected C is attributed to carbon injection on the examined surface before the XPS analysis. This observation is consistent with the results of the AES analysis (Fig. 9).

Figure 10b illustrates the XPS spectra for the Fe 2p regions. Fe 2p peaks are observed at the energy components of 710.87, 708.09 and 706.23 eV, these are consistent with the characteristic oxidized iron bonds of Fe_2O_3 and Fe_3O_4 [33]. Figure 10c shows the typical XPS spectra of the Si 2p regions. It reveals highly symmetric Si 2p signals with the binding energy of 103.62 eV. The absence of Si spectrum at the binding energy of 99.8 eV was reported [34], proving that Si exists exclusively in the oxidized state on the worn surface. The Si 2p spectra in Fig. 10c shows that the band

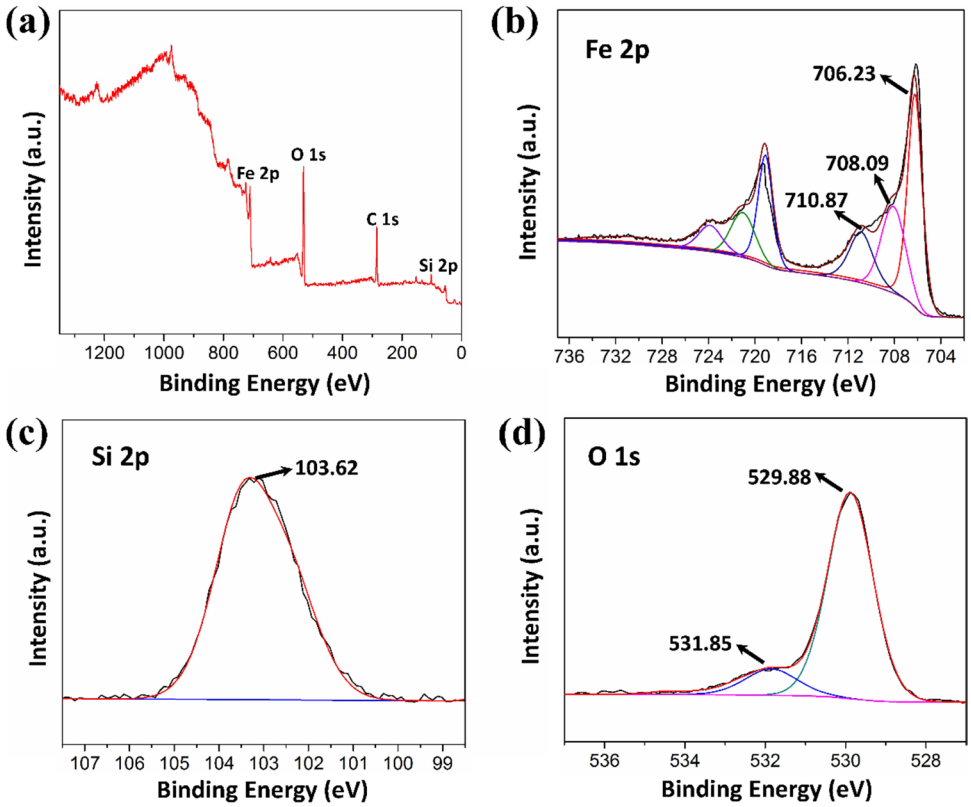

Fig. 10 X-ray photoelectron spectroscopy of the worn fish-scale film structure: **a** Full XPS survey spectrum, **b** Fe 2p peaks, **c** Si 2p peaks, and **d** O 1s peaks

at 103.62 eV corresponds to the standard binding energy of SiO_2 bonds [34, 35]. O 1s spectra in Fig. 10d shows that the fitting peak of O 1s is decomposed into two components, with the standard binding energy of 531.85 and 529.88 eV. Besides, the peak binding energy of 531.85 eV corresponds to the SiO_2 structure. The binding energy of 529.88 eV corresponds to the adsorbed O^{2-}, which is confirmed by Fe 2p and Si 2p peaks. The results of elemental and chemical analysis show that SiO_2 films in the worn fish-scale film structure are the main protective objects.

3.6 3D Worn Surface Morphology

Figure 11 shows the 3D morphology of DC53 steel with different surface types. Figure 11a–b, and d depict the specimens of as-received, quenched, and fish-scale film structures at a load of 50 N. The average width and depth of the wear traces on each corresponding surface are as follows: 292.6 and 21.9 µm (Fig. 11a), 0.6 and 3.7 µm (Fig. 11b), and 0.3 and 0.2 µm (Fig. 11d). For specimen with prefabricated fish-scale film structure, the average width and depth are 5.8 and 5.1 µm (Fig. 11c).

The worn profile of as-received specimen is wide and deep, with the roughest surface. For the quenched specimen, the sliding process results in numerous local plough scratches, characterized by a predominantly worn surface consisting of parallel shallow grooves. In addition, irregularly shaped granular debris is also observed. Deeper adhesive pits can be found on the as-received specimen surfaces, but this phenomenon is invisible on the fish-scale film structure surface, without adhesion wear (adhesion pits) and plow grooves. Compared with the as-received and quenched specimens, the fish-scale fim structure specimen exhibits optimal wear resistance at a load of 50 N. The change in wear resistance of the fish-scale film structure, produced by laser surface remelting, is independent of increased surface hardness compared to the wear morphology of quenched specimens.

3.7 Friction Coefficient and Wear Rate

Figure 12 compares the friction coefficients and worn volume losses corresponding to different wear loads. Figure 12a shows that as the load increases, the friction coefficient increases for as-received and quenched specimens. However, the increasing trend in quenched specimens is not as obvious as in the as-received. The friction coefficient of fish-scale film structure specimens is slightly lower than those of as-received and quenched specimens. Interestingly, it decreases with increasing load, in contrast to the changes in friction coefficients of as-received and quenched specimens. The fish-scale film structure shows the minimum friction coefficient at a load of 50 N.

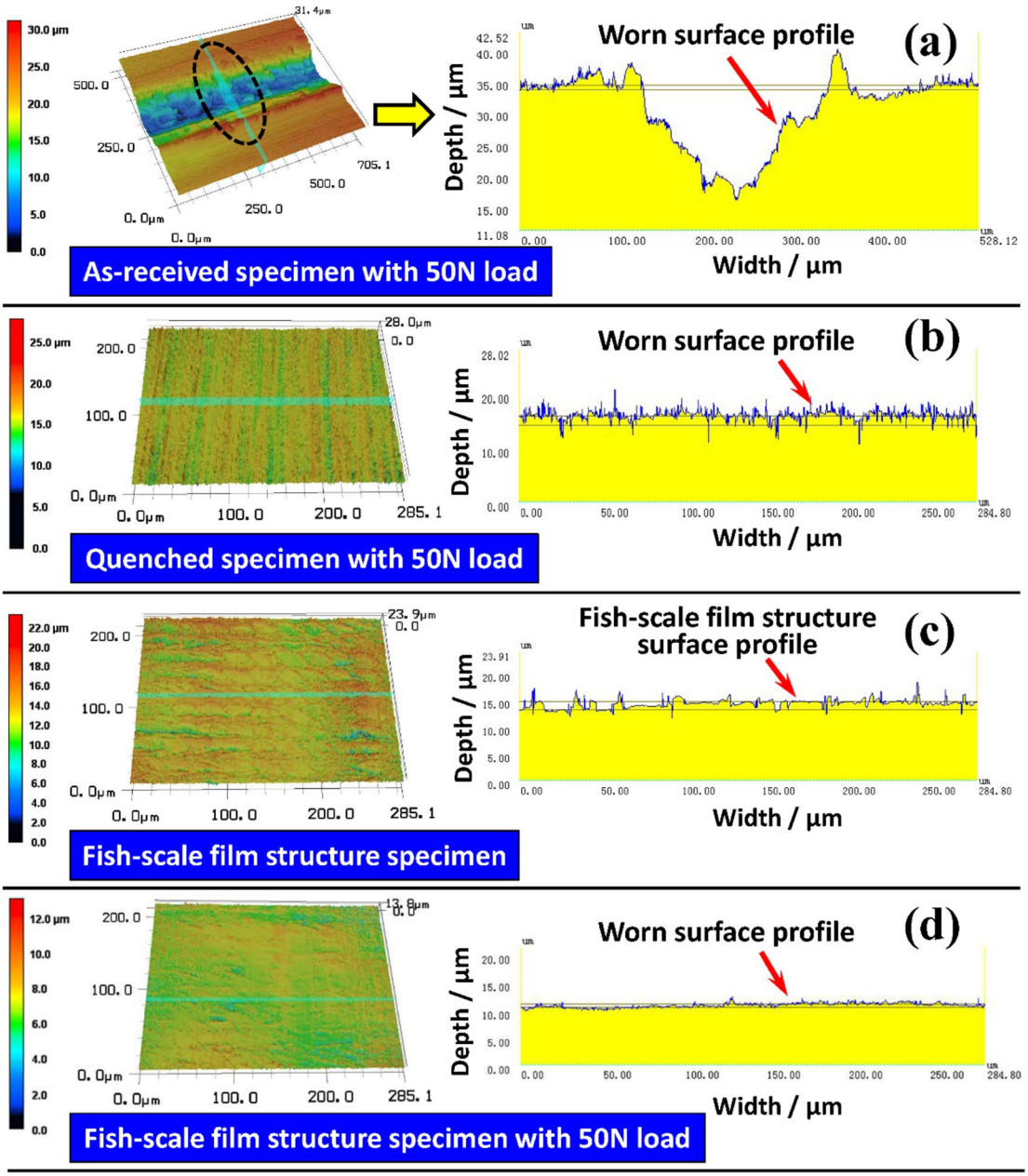

Fig. 11 3D worn surface morphologies at a load of 50 N for **a** as-received, **b** quenched; **c** prefabricated fish-scale film structure specimen; **d** worn surface morphology at a load of 50 N for fish-scale film structure specimen

The wear behavior of as-received specimens shows that the material has detached from the worn surface over a large area, accompanied by numerous adhesive pits. The adhesion effect occurs with a relatively high frequency. The detached surface and the adhesion effect are observed over a larger area at high loads. Therefore, the friction coefficient increases with increasing wear load.

Quenched specimens have high surface hardness and reinforced elastic layers. They are easy to produce elastic deformation in the wear process, which directly reduces the contact between the substrate and the coupling material. The adhesion effect and plow cutting caused by friction mainly occurs in the reinforced layer. In addition, the shear strength required to overcome the plastic deformation of the reinforced layer is not high enough. Thus, the increase in the friction coefficient is limited.

The friction coefficients of specimens with fish-scale film structures decrease with increasing load. This is attributed to the gradual spreading effects of SiO_2 particles on the friction process. The stable SiO_2 film layer, with the distribution of micro irregularities in the sliding area, acts as a self-lubricant. The friction-inducing adhesion and

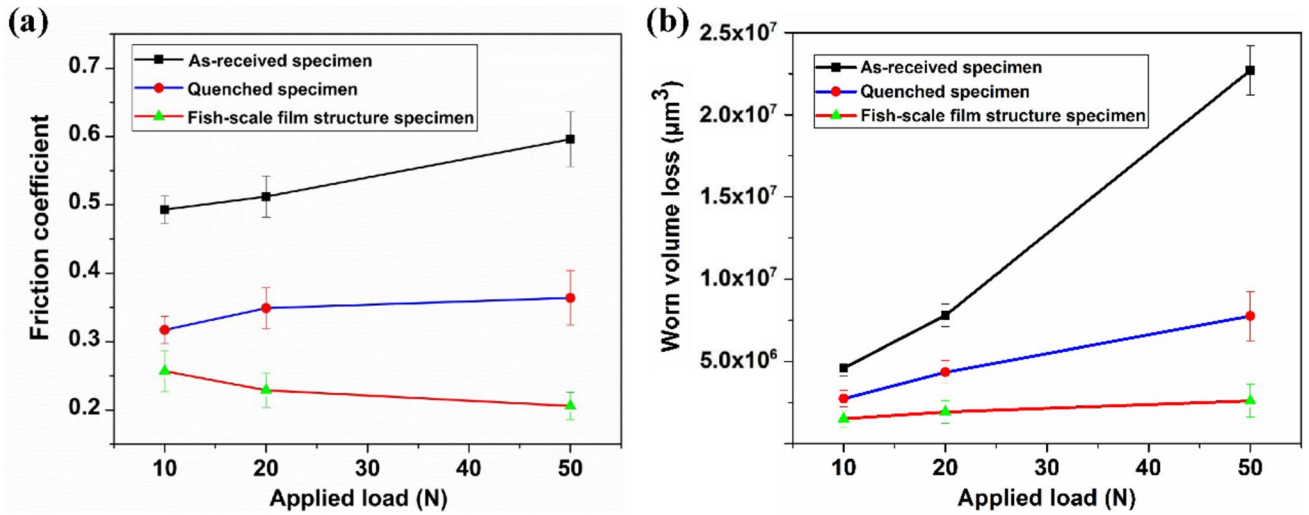

Fig. 12 Variations of friction coefficients and worn volume losses with loads for specimens of as-received, quenched, and fish-scale film structures: **a** friction coefficients versus loads; **b** worn volume losses versus loads

plowing effect mainly occur in the SiO_2 protective film. The shear strength required to overcome the plastic deformation of the film structure is reduced. Thus, the friction coefficient decreases.

Figure 12b shows worn volume losses corresponding to different loads. The change in worn volume loss is similar to that of the friction coefficients mentioned as-received and quenched specimens.

The as-received specimens have the largest worn volume loss under the same loading conditions. The worn volume loss of quenched specimens increases slowly compared with the as-received specimens under the increased load. Furthermore, the worn volume loss of the fish-scale film structure increases slowly compared with the as-received and quenched specimens. At a load of 50 N, the as-received specimens show a worn volume loss that is seven times larger than that of the fish-scale film structure. Meanwhile, the fish-scale film structure has the lowest wear load factor and an excellent protective effect on the worn volume loss, it is more suitable under high load, and the "polishing effect" appears on the worn surface.

The furrow effect of the as-received specimen surface is coarse, and a severe shear tear deformation can be seen on the friction surface, which leads to the high worn volume loss. The increased worn volume loss of quenched specimen is due to the stronger adhesion between the friction pairs and the interaction at the local contact points. It obstructs the relative movement between the mating surfaces.

However, the thick reinforcing layer in quenched specimen protects against further abrasion due to the solid solution strengthening, dispersion strengthening, and grain refinement achieved through the quenching process. The lower shear strength of the quenched layer reduces the adhesive abrasion, resulting in weak shear force, as compared with the as-received specimens.

The dispersion of hard SiO_2 particles on the worn surface softens the direct contact between the film structure and the friction pair in the fish-scale film structure specimen, thereby reducing adhesion. As the primary shear stress is maintained by the SiO_2 particles, the depth of the micro protrusions from the worn surface decreases. This also reduces plastic deformation in the fish-scale film structure's subsurface layer and increases its wear resistance at high loads. When some SiO_2 films spread, a continuous supply of new SiO_2 protected film catches up with the newly worn surface. The adhesion process is defined by the interaction of two phases, the plastic extrusion and micron-film structural adjustment, within a confined region. All of these effects lead to the lowest worn volume loss of the fish-scale film structure specimen.

3.8 Tribological Mechanism

Due to the non-ideal smoothness of the actually worn contact surface in the wear test, there is an interplay between micro-convex bodies at the friction pair interface (Fig. 13a). When subjected to wear, elastic or plastic deformation occurs in the contact area. This results in abrasive and adhesive wear in the contacted convex body. The combined convex body reduces in tearing under the shearing action during the sliding process. These factors increase the friction coefficient and wear rate in as-received specimens.

For specimens with fish-scale film structure, as the load increase, the worn layer contacts the bulge profile at the boundary of the special structure (Fig. 13b). The direct contact between the whole body of the fish-scale

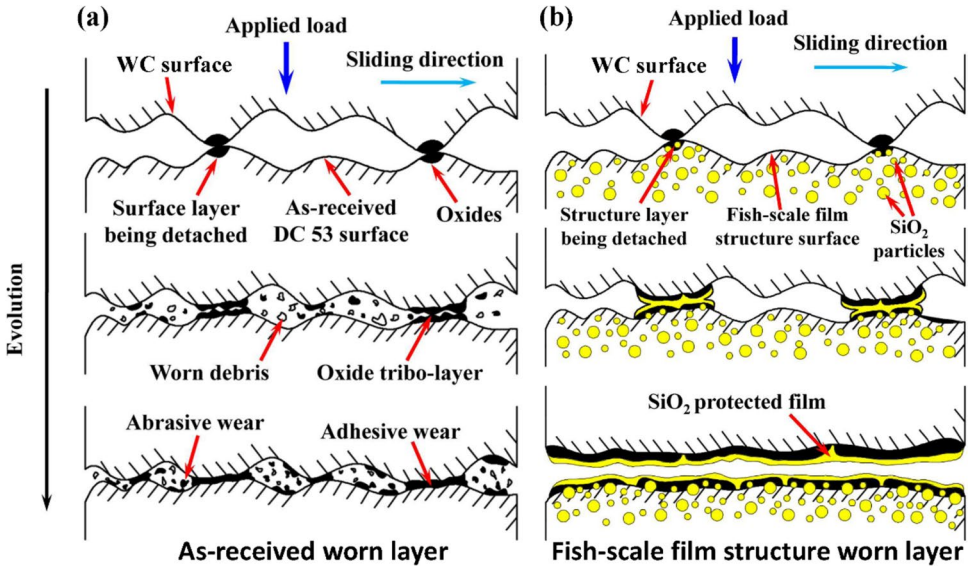

Fig. 13 Schematic diagrams of the wear mechanism of the as-received and fish-scale film structure: **a** as-received; **b** fish-scale film structure

film structure and the WC ball is reduced, resulting in less adhesive wear. Once the increased SiO_2 particles with enhanced strength and hardness adhere to the worn surface, these particles serve as the effective pinning points. It prevents the movement of materials on the real worn contact surface, which forms a plugging area. These hard SiO_2 precipitates appear as hillock morphology on the worn surface when they are not completely crushed by the upper friction pair (Fig. 7a).

The size and duration of the plugging area depends on the bearing capacity of the SiO_2 particles. When the applied load exceeds the particles' bearing capacity, SiO_2 fragments will be spalled. Then the plugging area is easily filled into exfoliation, which leads to the clamping and covering of SiO_2 particles. The SiO_2 particles bear the frictional load and are broken with the plugging zone decomposed during the friction process. Consequently, the plugging area experiences plugging, covering, decomposition, re-plugging, and recovery.

At higher loads, the WC ball applies forward pressure and tangential plowing force to SiO_2 particles on the friction surface. These SiO_2 particles are partially crushed and fragmented into smaller particles. The fractures of smaller SiO_2 particles increase with the increased load, which causes pulverized damage. Then these particles are extruded into a dense state, and the compaction degree increases with the increased loads. Finally, the self-lubrication process results in the formation of protective SiO_2 film (Fig. 13b). This protective film lessens the plowing resistance of the film structure. Meanwhile, fragmented SiO_2 particles slide and absorb into the worn surface, which reduces their sharpness and furrow effect as well as the friction coefficient and worn volume variations of the fish-scale film structure specimens.

4 Conclusions

A regular distributed fish-scale film structure formed by laser remelting was studied to improve the wear resistance of DC53 steel. Comparative tests were carried out on as-received, quenched, and fish-scale film structure specimens to exclude increased wear resistance caused by the quenching effect. Differences and regularities were compared in worn surface morphology and volume loss, friction coefficient, structural composition, and element distribution at different friction loads. The formation mechanism of tribo-layers was proposed. The main conclusions are listed as follows:

1. As the wear load increased, the plow ditch and peeling phenomenon increased significantly in the as-received specimen. The wear mechanism was manifested as plowing ditches and adhesive wear at the break-in stage. Quenching resulted in grain refinement and solid phase enhancement of the material structure, this resulted in the lower shear strength of the friction layer with excellent plastic deformation, which reduced the worn volume of the quenched samples. The combined effects of these factors made the friction coefficient of quenched samples being lower than that of the as-received. The friction coefficient decreases rapidly, accompanied by a slight accessorial volume loss of the fish-scale film structure speicmens with the increased load. Meanwhile, the wear surface exhibited a dense, flat and remarkably

smooth texture, and showed excellent abrasion resistance to frictional damage caused by high load movements.

2. EDS, EPMA, AES, and XPS results showed that the SiO_2 protective film formed on the worn surface of the fish-scale film structure. Based on the analysis of the microstructure and chemical composition, tribo-layers were formed during sliding. SiO_2, one of the main chemical compositions in tribo-layers, inhibited the friction.
3. The influence of SiO_2 particles on the friction coefficients and wear performance was closely related to the wear loads. Although the impact of SiO_2 particles content on the friction coefficient was obvious at low load, the wear rate remained unaffected by fluctuations in SiO_2 content. High load caused an increase in SiO_2 particles, resulting in the dispersion of fractured SiO_2 particles into the sub-layer, which was characterized by a severely weakened plow ditch. A dynamic balance was achieved between the formation and peeling of trace amounts of SiO_2 protective films on the worn surface, which resulted in a consistently low and stable friction coefficient and wear rate. Consequently, the fish-scale film structure exhibited lower friction coefficients and worn volume than both the as-received and quenched specimens at various wear loads.

Acknowledgements We would like to express our deep gratitude to the IPG Photonics Corporation for their cooperation and support in fabricating the structures studied in this work. We also thank the Analysis and Test Center of Huazhong University of Science and Technology), for their testing service. This work was funded by the Chinese National Science and Technology Major Project (Item No. 2018YFB1106), and the key laboratory fund project of Hubei Key Laboratory of Digital Textile Equipment, Wuhan Textile University (Grant No. DTL2023015, KDTL2023006).

Data availability All data generated or analyzed during this study are included in this published article.

Declarations

Conflict of Interest The authors declare that they have no known competing financial interests or personal relationships that could have appeared to influence the work reported in this paper.

References

1. Kanlayasiri, K., & Boonmung, S. (2007). Effects of wire-EDM machining variables on surface roughness of newly developed DC 53 die steel: Design of experiments and regression model. *Journal of Materials Processing Technology, 192*, 459–464. https://doi.org/10.1016/j.jmatprotec.2007.04.085
2. Rehman, M., Khan, S. A., & Naveed, R. (2020). Parametric optimization in wire electric discharge machining of DC53 steel using gamma phase coated wire. *Journal of Mechanical Science and Technology, 34*(7), 2767–2773. https://doi.org/10.1007/s12206-020-0609-2
3. Kanlayasiri, K., & Boonmung, S. (2007). An investigation on effects of wire-EDM machining parameters on surface roughness of newly developed DC53 die steel. *Journal of Materials Processing Technology, 187*, 26–29. https://doi.org/10.1016/j.jmatprotec.2006.11.220
4. Kanlayasiri, K., Jattakul, P., & Mookam, N. (2022). Machinability of tool steels machined by electric-discharge machining. *Creative Science*, *14*(1), 25–31. https://doi.org/10.55674/snrujst.v14i1.244172
5. Mao, D., Wang, X., Wang, W., & Wei, X. (2012). Effect of boronizing on the dry sliding wear behavior of DC53/0.45 mass% C steel pairs. *Surface and Coatings Technology, 207*, 190–195. https://doi.org/10.1016/j.surfcoat.2012.06.061
6. Wen, D.-C. (2010). Erosion and wear behavior of nitrocarburized DC53 tool steel. *Wear, 268*(3–4), 629–636. https://doi.org/10.1016/j.wear.2009.10.012
7. Hassan, S., Khan, S. A., Naveed, R., Saleem, M. Q., Mufti, N. A., & Farooq, M. U. (2023). Investigation on tool wear mechanisms and machining tribology of hardened DC53 steel through modified CBN tooling geometry in hard turning. *The International Journal of Advanced Manufacturing Technology, 127*, 547–564. https://doi.org/10.1007/s00170-023-11528-5
8. Aramaki, M., Yamada, N., & Furukimi, O. (2011). Effect of combined shot treatment and nitriding on galling property of die used for high strength steels. *ISIJ international, 51*(7), 1137–1141. https://doi.org/10.2355/isijinternational.51.1137
9. Wang, W., Zheng, X., Hua, M., & Wei, X. (2016). Influence of surface modification on galling resistance of DC53 tool steel against galvanized advanced high strength steel sheet. *Wear, 360–361*, 1–13. https://doi.org/10.1016/j.wear.2016.04.021
10. Cora, Ö. N., Ağcayazı, A., Namiki, K., Sofuoğlu, H., & Koç, M. (2012). Die wear in stamping of advanced high strength steels – Investigations on the effects of substrate material and hard-coatings. *Tribology international, 52*, 50–60. https://doi.org/10.1016/j.triboint.2012.02.016
11. Kim, J., Chun, D.-M., Park, H. W., & Kim, J. (2023). Waterproof and Wear-Resistant Surface Treatment on Printed Parts of Polyamide 12 (PA12) by Selective Laser Sintering Using a Large Pulsed Electron Beam. *International Journal of Precision Engineering and Manufacturing-Green Technology, 10*(1), 71–83. https://doi.org/10.1007/s40684-022-00420-4
12. Li, L., Li, Z., Xing, Z., Guo, W., Huang, Y., & Wang, H. (2023). Effect of femtosecond laser bionic texture on anti-wear properties of medical Ti-6Al-4 V. *Tribology international, 190*, 109062. https://doi.org/10.1016/j.triboint.2023.109062
13. Xing, Y., Deng, J., Wu, Z., & Wu, F. (2017). High friction and low wear properties of laser-textured ceramic surface under dry friction. *Optics & Laser Technology, 93*, 24–32. https://doi.org/10.1016/j.optlastec.2017.01.032
14. Lian, Z., Cheng, Y., Xu, J., Xu, J., Ren, W., Tian, Y., & Yu, H. (2023). Green fabrication of anti-friction slippery liquid-infused metallic surface with sub-millimeter-scale asymmetric bump arrays and its application. *International Journal of Precision Engineering and Manufacturing-Green Technology, 10*(5), 1281–1298. https://doi.org/10.1007/s40684-022-00463-7
15. Guo, Z., Guo, B., Zhao, Q., Zeng, Z., & Xu, L. (2023). Wear characteristics of micro-structured CVD diamond grinding tools. *Wear, 514–515*, 204569. https://doi.org/10.1016/j.wear.2022.204569
16. Dai, F. Z., Geng, J., Tan, W. S., Ren, X. D., Lu, J. Z., & Huang, S. (2018). Friction and wear on laser textured Ti6Al4V surface subjected to laser shock peening with contacting foil. *Optics & Laser Technology, 103*, 142–150. https://doi.org/10.1016/j.optlastec.2017.12.044

17. Li, X., Deng, J., Lu, Y., Duan, R., & Ge, D. (2022). Machinability investigation and sustainability assessment of dry cutting AISI1045 steel using tools configured with shark-skin-inspired structures and WS2/C coatings. *International Journal of Precision Engineering and Manufacturing-Green Technology, 9*(1), 83–106. https://doi.org/10.1007/s40684-021-00330-x
18. Qiu, Y., Liu, W., Jin, L., Ye, Z., Chen, J., & Wang, Y. (2023). Picosecond laser-textured WC-10Co4Cr metal-ceramic composite coatings with high wear resistance property. *Surface and Coatings Technology, 474*, 130073. https://doi.org/10.1016/j.surfcoat.2023.130073
19. Liu, X., Guo, Z., Lu, Z., & Qin, L. (2023). Tribological behavior of the wear-resistant and self-lubrication integrated interface structure with ordered micro-pits. *Surface and Coatings Technology, 454*, 129159. https://doi.org/10.1016/j.surfcoat.2022.129159
20. Lu, L., Zhang, Z., Guan, Y., & Zheng, H. (2018). Comparison of the effect of typical patterns on friction and wear properties of chromium alloy prepared by laser surface texturing. *Optics & Laser Technology, 106*, 272–279. https://doi.org/10.1016/j.optlastec.2018.04.020
21. Jia, X., Zhang, Y., Dong, X., & Wang, Z. (2024). Enhanced lipophilicity and wear resistance of 20CrMnTi induced by laser surface texturing. *Optics & Laser Technology, 170*, 110329. https://doi.org/10.1016/j.optlastec.2023.110329
22. Wang, W., Yuan, W., Guo, Q., Wang, N., Chi, B., & Yu, J. (2024). Effect of picosecond laser surface texturing under Babbitt coating mask on friction and wear properties of GCr15 bearing steel surface. *Engineering Failure Analysis, 157*, 107878. https://doi.org/10.1016/j.engfailanal.2023.107878
23. Lu, G., Sokol, D. W., Zhang, Y., & Dulaney, J. L. (2019). Nanosecond pulsed laser-generated stress effect inducing macro-micro-nano structures and surface topography evolution. *Applied Materials Today, 15*, 171–184. https://doi.org/10.1016/j.apmt.2019.01.005
24. Pan, X., Zhou, L., Hu, D., He, W., Liu, P., Yu, Z., & Liang, X. (2023). Superior wear resistance in cast aluminum alloy via femtosecond laser induced periodic surface structures and surface hardening layer. *Applied Surface Science, 636*, 157866. https://doi.org/10.1016/j.apsusc.2023.157866
25. Pfefferkorn, F. E., & Morrow, J. D. (2017). Controlling surface topography using pulsed laser micro structuring. *CIRP Annals, 66*(1), 241–244. https://doi.org/10.1016/j.cirp.2017.04.138
26. Temmler, A., Willenborg, E., & Wissenbach, K. (2011). Design surfaces by laser remelting. *Physics Procedia, 12*, 419–430. https://doi.org/10.1016/j.phpro.2011.03.053
27. Bordatchev, E. V., Küpper, M., Cvijanovic, S. J., Willenborg, E., Milliken, N., Temmler, A., & Tutunea-Fatan, O. R. (2020). Edgelit sine-shape wedged light guides: Design, optical simulation, laser-remelting-based precision fabrication, and optical performance evaluation. *Precision Engineering, 66*, 333–346. https://doi.org/10.1016/j.precisioneng.2020.07.004
28. Temmler, A., & Pirch, N. (2020). Investigation on the mechanism of surface structure formation during laser remelting with modulated laser power on tool steel H11. *Applied Surface Science, 526*, 146393. https://doi.org/10.1016/j.apsusc.2020.146393
29. Temmler, A., Pirch, N., Luo, J., Schleifenbaum, J. H., & Häfner, C. L. (2020). Numerical and experimental investigation on formation of surface structures in laser remelting for additive-manufactured Inconel 718. *Surface and Coatings Technology, 403*, 126370. https://doi.org/10.1016/j.surfcoat.2020.126370
30. Temmler, A., Dai, W., Schmickler, T., Küpper, M. E., & Häfner, C. L. (2021). Experimental investigation on surface structuring by laser remelting (WaveShape) on Inconel 718 using varying laser beam diameters and scan speeds. *Applied Surface Science, 541*, 147814. https://doi.org/10.1016/j.apsusc.2020.147814
31. Kreinest, L., Schober, B., Willenborg, E., & Stollenwerk, J. (2024). Investigation of asymmetry reduction for surface structuring and destructuring by laser remelting. *Heliyon, 10*(2), e24067. https://doi.org/10.1016/j.heliyon.2024.e24067
32. Dai, W., Zhang, W., Zheng, Z., & Li, J. (2019). Investigation of micron-sized fish-scale surface structures on tool steel surfaces using laser galvanometer scanning. *Applied Surface Science, 470*, 1111–1121. https://doi.org/10.1016/j.apsusc.2018.10.264
33. Graat, P. C. J., & Somers, M. A. J. (1996). Simultaneous determination of composition and thickness of thin iron-oxide films from XPS Fe 2p spectra. *Applied Surface Science, 100*, 36–40. https://doi.org/10.1016/0169-4332(96)00252-8
34. Alfonsetti, R., Lozzi, L., Passacantando, M., Picozzi, P., & Santucci, S. (1993). XPS studies on SiOx thin films. *Applied Surface Science, 70*, 222–225. https://doi.org/10.1016/0169-4332(93)90431-A
35. Alfonsetti, R., De Simone, G., Lozzi, L., Passacantando, M., Picozzi, P., & Santucci, S. (1994). SiOx surface stoichiometry by XPS: A comparison of various methods. *Surface and interface analysis, 22*(1–12), 89–92. https://doi.org/10.1002/sia.740220122

Wei Dai received the Ph.D. degree in School of Materials Science and Engineering from Huazhong University of Science and Technology, Wuhan, China in 2020. He is currently working in the School of Mechanical Engineering and Automation, Wuhan Textile University, China. His current research interests include laser material processing, microstructure manufacturing and surface engineering.

Chuqiao Fang Master in the School of Mechanical Engineering and Automation, Wuhan Textile University, Wuhan, China. His research interests include laser surface manufacturing, surface processing technology.

Xiao Wu received the Ph.D. degree in School of Materials Science and Engineering from Huazhong University of Science and Technology, Wuhan, China in 2011. Currently he is a professor in the Schoolof Mechanical Engineering and Automation, Wuhan Textile University, China. His research interests focus on precision microforming technology, precision mold design theory and manufacturing.

Zhizhen Zheng received the Ph.D. degree in School of Materials Science and Engineering from Huazhong University of Science and Technology, Wuhan, China in 1999. He is an associate professor in the School of Materials Science and Engineering at Huazhong University of Science and Technology, China. His research interests include in mold and die digital manufacturing, large die forging process.

Jianjun Li received the Ph.D. degree in School of Materials Science and Engineering from Huazhong University of Science and Technology, Wuhan, China in 1995. Currently he is a professor in the School of Materials Science and Engineering at Huazhong University of Science and Technology. His research interests focus on advanced mold processing and manufacturing technology. He had worked as the supervisor of the State Key Laboratory of Materials Processing and Die & Mould Technology at Huazhong University of Science and Technology.